International Journal of Heat and Mass Transfer 97 (2016) 868–879

Contents lists available at ScienceDirect

International Journal of Heat and Mass Transfer

journal homepage: www.elsevier.com/locate/ijhmt

Heat transfer augmentation in rectangular micro channel covered with vertically aligned carbon nanotubes

T.J. Taha [a,*], L. Lefferts [b], T.H. van der Meer [a]

[a] Thermal Engineering, Faculty of Engineering and Technology, University of Twente, 7500 AE Enschede, Netherlands
[b] Catalytic Processes and Materials, Faculty of Science and Technology, University of Twente, 7500 AE Enschede, Netherlands

ARTICLE INFO

Article history:
Received 21 May 2015
Received in revised form 25 January 2016
Accepted 7 February 2016
Available online 14 March 2016

Keywords:
MWCNTs
Enhancement
Heat transfer
Microchannel
Surface roughness
Scaling effect

ABSTRACT

An experimental heat transfer investigation was carried out to examine the influence of carbon nanotubes (CNTs) layer deposits on the convective heat transfer performance inside rectangular microchannels. Successful synthesis of vertically aligned CNTs was achieved using a catalytic vapor deposition (CVD) process on a silicon sample substrate. By varying the synthesis time, on average 6 μm and 20 μm thick layers of CNTs were made with surface roughness of (S_a = 1.062 μm, S_q = 1.333 μm) and (S_a = 0.717 μm, S_q = 0.954 μm) respectively. The external surface area of the samples increased 7 times compared to the bare silicon chip. The heat transfer performance of each sample was measured inside two rectangular microchannels with cross-section of 125 μm × 9 mm and 200 μm × 9 mm. For the 125 μm channel height, the 6 μm and 20 μm thick layer of CNTs resulted in 12% and 26% increase in pressure drop respectively. The pressure drop obtained from the 200 μm channel height show a similar trend with an increase of 6% and 16.4% for 6 μm and 20 μm CNTs layer thickness respectively. An average heat transfer enhancement of 19% and 74% is obtained inside the 125 μm height microchannel with 6 μm and 20 μm CNTs layer thickness respectively. Whereas, the average heat transfer enhancement of 22% and 62% are obtained inside the 200 μm channel with respective CNTs layer thicknesses of 6 μm and 20 μm. Enhancements are attributed to an increase in surface area and effective thermal conductivity inside the thermal boundary layer. However, the frictional heating (viscous dissipation) of a particular nanostructured sample increases with a decrease in channel height. This difference in channel size results in stronger competition between heat transfer enhancement potential that can be achieved by the deposited surface and the decrease in Nusselt number due to viscous dissipation.

1. Introduction

Recent advancement in microfabrication leads to new micro-scale devices such as micro-chips [1–3], micro-biochip [4–6], lab-on-chip [7–10], micro-reactors [11–13] and micro-fuel cells [14–17]. The miniaturizing trend has significantly increased the heat dissipation from the immerging technologies. The need for effective and efficient cooling technologies, especially in micro-flow devices, motivates the heat transfer research community to conduct intensive and extensive research in microchannel heat transfer. Some of the application areas are in the development of micro-heat sink, micro-scale sensing and measurement, micro-electro-mechanical systems (MEMS), micro compressors and biotechnology. Moreover, the classical heat transfer enhancement methods, both active [18–21] and passive [22–27], are used to further enhance heat dissipation potential of the heat transfer surfaces. Due to the outstanding thermal and mechanical properties, carbon nanotubes (CNTs) are considered as a promising material in heat transfer research [28–31].

Kordas et al. [32] have reported an efficient chip cooling by integrating both laser patterned CNT and copper micro fin structures on a silicon chip. Heat transfer enhancement results were reported for both CNTs and copper structures for both natural and forced convection with an enhancement of 11% and 19% respectively. However, an un-patterned CNTs layer shows poor heat transfer performance due to the dense nature of the CNTs layer hampering the flow of N_2 in the film, limiting the heat transfer only to the upper facet of the films, resulting in limited cooling capabilities. It is also suggested that by changing fin geometry, dimension and fin densities more efficient cooling can be achieved.

Zhimin Mo et al. [33] reported effective cooling for microelectronic applications using integrated CNT fins made by lithographic technique and CVD on a micro-channel surface. It was mentioned

* Corresponding author.
E-mail addresses: t.j.taha@utwente.nl, taha.jibril.taha@gmail.com (T.J. Taha).

http://dx.doi.org/10.1016/j.ijheatmasstransfer.2016.02.039
0017-9310/

Nomenclature

W	width of the rectangular micro-channel [m]
H	height of the rectangular micro-channel [m]
γ	heat capacity ratio = 1.4 [–]
R	specific gas constant = 287.058 [J/(kg K)]
A_c	cross-sectional area [m^2]
D_h	hydraulic diameter of the channel [m]
$\bar{U}$	average flow speed [m/s]
ΔP	pressure difference [Pa]
l	length of the sample [m]
T_2	average air temperature exiting the sample [K]
T_1	average air temperature entering the sample [K]
T_s	sample surface temperature [K]
k_w	wall thermal conductivity [W/(m K)]
k_f	thermal conductivity of air at film temperature [W/(m K)]
μ_f	dynamic viscosity of air at film temperature [Pa s]
ρ_f	density of air at film temperature [kg/m^3]
Cp_f	specific heat at film temperature [kJ/Kg K]
i	electrical current [A]
V	voltage drop across the wire [V]
ΔT_{LMTD}	logarithmic temperature difference [K]
h	heat transfer coefficient [W/(m^2 K)]
$\dot{m}$	mass flow rate [m^2]
A	heat transfer surface area [m^2]
Re	Reynolds number [–]
$\overline{Nu}_{Dh}^{Bare}$	Nusselt number with bare channel hydraulic diameter [–]
$\overline{Nu}_{Dh}^{CNTs}$	Nusselt number with corrected channel hydraulic diameter [–]
f	friction factor [–]
Ma	Mach number [–]
S_a	average surface roughness [m]
S_q	root mean square of the surface roughness [m]
η_T	heat transfer enhancement [–]
η_p	pressure penalty [–]
Pe	Peclet number [–]
Pr	Prandtl number [–]
Gz	Graetz number [–]
Br	Brinkman number [–]
ϵ	relative surface roughness [–]
cf	constricted flow
N	number of statistical samples [–]
Z	sample height data [m]

that the flow rates were decreased by 12% whereas the heating power input is increased by 23% keeping the transistor temperature 6 °C below the reference cooler. It was also suggested that self-aligned CNTs would increase the heat transfer even more than what was achieved.

Shenoy et al. [34] experimentally determined the heat removal potential of multi-walled carbon nanotubes (MWCNTs) grown in silicon mini-channel with water as a cooling medium. At constant temperature boundary condition, heat flux enhancement of 2.3 and 1.6 times, compared to a device without MWCNTs was reported for MWCNT bundles and fully covered MWCNTs respectively. Further investigation were made by Tullius et al. [35] to investigate the combined influence of a Al_2O_3/H_2O nanofluid and MWCNTs on the heat transfer performance in the same setup. Little to no enhancement was obtained by using the combined nano-fluid in both fully covered and bundles of MWCNTs.

Tuzovskaya et al. [36] performed experimental investigations on stainless steel and on carbon foam. CNT's on stainless steel resulted in enhancement of heat transfer ranging from 30–75%, while CNT's on carbon foam decrease heat transfer by 40%. It was explained that the cumulative effect of an increase of heat exchange surface area, the structural arrangement of the graphene layer and the higher crystallinity results in the overall performance of the stainless steel foam.

Previously, Taha et al. [37,38] investigated the influence of CNFs layer morphology on convective heat transfer for a 50 μm diameter nickel wire. Three morphologically different samples were investigated which resulted in heat transfer enhancement in an open structure and a decrease in heat transfer in the densely populated layer CNFs. Furthermore, a highly crystalline sample with rough surface morphology resulted in an exceptional enhancement of 34%. A follow-up investigation was made to investigate the indirect involvement of the a-C layer on convective heat transfer enhancement using CNFs [39] which indicates the existence of an optimum layer thickness.

The aim of this work is to experimentally investigate the influence of CNTs layer on convective heat transfer behavior inside rectangular micro-channels. Synthesis of vertically aligned carbon nanotubes (VACNTs) was made on a silicon chip with integrated Platinum (Pt) thin film heater. Different CNTs layer thicknesses were synthesized and surface characterizations were made. The influence of the layer thickness with respect to the hydraulic diameter is further investigated.

2. Experiments

2.1. CNTs synthesis

2.1.1. Thin film deposition

The controlled pretreatment and synthesis parameters of the carbon nanostructures determines the size of the catalytic metal particles, length of the fibers, shape, graphene layer arrangement and diameter of the fibers, which influences the porosity, permeability, thermal conductivity, surface area and roughness of the layer produced. Tailoring these parameters creates a novel material with exceptional thermal, mechanical, electrical and physical properties that can be used in variety of applications.

Silicon samples (10 mm × 10 mm) are designed to accommodate the synthesis of the VACNTs and aid in measuring the convective heat transfer performance. This is achieved by depositing two different layers to the two opposite faces of the silicon wafer. The catalytic material used for the synthesis process is deposited on one side of the wafer in an area of 10 mm × 8 mm, and a thin film electrical heater is deposited on the other side of the wafer.

Thermal catalytic vapor deposition (TCVD) process is the method used to facilitate the decomposition of hydro-carbon gases on active catalytic component such as transition metals. The current study uses a thin layer of Iron (Fe) as catalyst surface. However, physical vapor deposited Fe does not adhere well to materials such as silicon, quartz and fused silica. As a result, a thin adhesive layer between the Fe and silicon substrate material has to be used [40]. A similar adhesive layer is required between the Pt thin film heater and the silicon substrate. For high temperature application (exceeding 500 °C), titanium and tantalum are often used as an adhesion material [41,42].

The substrate used in this study is 100 mm ⟨100⟩ oriented silicon wafer with double side polished (thickness of 525 μm thick, p type, Resistivity: 5–10 Ωcm). Using de-mineralized water, the substrates were ultrasonically cleaned, followed by immersion of the

substrate in 99% nitric acid for 10 min, and quick dump rinsing it in demineralized water. The substrate were further boiled (95 °C) in 69% nitric acid for 10 min, followed by quick dump rinsing in demineralized water in order to remove trances of the cleaning agent, and dry spinning it. After the dry spinning process, the substrate was placed in dehydration bake (95 °C, 5 min) in order to remove the traces of moisture. A thin layer of SiO_2 was thermally produced on both sides of the silicon wafer. This thin layer is used as an electrical insulation for the Ta/Pt heater from the silicon.

Thin film metal deposition was made *via* evaporation and sputtering. Using Balzers BAK600 electron gun evaporation system, Ta (10 nm)/Fe (5 nm) films were deposited at a pressure less than 10^{-6} mbar on one side of the wafer. The evaporation rate of both Ta and Fe layer were in the range of 1–20 Å/s. The thickness of the layers deposited is determined using in-situ thickness monitoring.

Using Sputterke (a film sputtering device), Pt/Ta films were deposited by making use of argon to adjust the sputtering pressure to 6.6×10^3 mbar. The target purity of Pt was 99.99% and 99.9% for Ta. A 180 nm thick layer of Pt was deposited at a sputtering rate of 22–27 nm/min while a 10 nm thick Ta layer was deposited at a rate of 16.5 nm/min. The sputtered metal layer thickness was estimated based on a calibration run performed prior to the actual sputtering process. Post to sputtering, ultrasonic lift-off was performed (20 min) using acetone followed by immersion of the wafer into isopropanol (10 min), dehydration bake at hot plate (120 °C for 5 min). Prior to dicing, a photo resistive layer was spin coated to protect the surface from contamination during dicing.

2.1.2. CNTs synthesis setup and process

Prior to the synthesis of the VACNTs, the Iron based thin film samples were first cleaned ultrasonically in acetone (10 min, HBM ultrasonic cleaner) to remove the protective photoresist film, then rinsed in isopropanol and dryed with pressurized air. Subsequently, the samples were placed with the Fe film facing upward inside a horizontally oriented, 45 mm diameter, TCVD quartz reactor.

The samples were reduced in 20 vol.% of H_2 (99.999%, INDUGAS) in N_2 (99.999%, INDUGAS) with a total flow rate of 50 ml/min, while increasing the temperature to 720 °C at a rate of 10 °C/min and maintaining the temperature for a total period of 3 h. This pretreatment condition is essential in creating nucleation sites of the synthesis of CNTs by de-wetting of the Fe thin film, thus creating nano-particles. Following the pretreatment process, the samples were flushed with N_2 at flow rate of 100 ml/min for 10 min. in order to remove H_2 from the reactor. The samples were further exposed to 33.33 vol.% ethylene (C_2H_4, 99.95% PRAXAIR) in N_2 at a total flow rate of 150 ml/min. In order to obtain two different heights of CNTs, two different synthesis periods were chosen (45 min and 90 min). Finally samples were cooled down naturally (turning off the furnace) in N_2, 100 ml/min.

2.2. Microchannel setup

A micro-channel heat transfer setup is carefully designed to investigate the influence of the produced micro- and nano-structured materials on convective heat transfer and pressure drop. The main body of the setup is made up of PEEK, a polymer with various advantages such as low thermal conductivity, high thermal stability, high strength coupled with toughness. PEEK has often been used as a substitute for metals in a number of engineering applications such as bearings, piston parts and pumps. Fig. 1 shows the exploded view of the setup and every component is visible with a detailed sectional view of the assembled component. The full dimension of the setup is $L \times W \times H$ $124 \times 49 \times 45$ mm. The width of the rectangular channel is designed to be 9 mm whereas the height of the channel depends on the thickness of the foil used. Thus, by changing the size of the PEEK foil, the setup provides flexibility of channel height, which helps to investigate the influence of the same nano-structural materials with different aspect ratio. Two channels with height of 125 μm and 200 μm were used resulting in aspect ratio's of 72 and 45 respectively. The hydraulic diameter for the rectangular microchannel is calculated as:

$$D_h = \frac{4A_c}{P} = \frac{4W \cdot H}{2(W+H)} \tag{1}$$

Prior to assembling the micro-channel setup, each component including the internals of the channel is cleaned with isopropanol, which helps in removing small particles and dusts. The Pt heater deposited at the bottom of the silicon sample has two pads for electrical connections extending 1 mm throughout the edge of the samples. The remaining surface has been deposited with Pt in a zigzag formation with a strand width of 100 μm and 125 μm spacing. During assembly the two electrical connections of the samples are placed directly on top of the copper electrodes. Through these electrodes the sample is supplied with electrical current, which is used to heat the sample. The clean PEEK foil and top block are carefully placed on top of the sample. The foil used creates the micro-channel needed and determines the channel size used in the experiment. Subsequently, the top and bottom stainless steel blocks are used to clamp the micro-channel. The channel surface roughness (RMS) was measured to be in the range of 320–477 nm. This surface roughness has negligible impact on the micro-channel flow characteristics. The sample is located at a distance of 35.5 mm away from the inlet port. At the location of the sample the flow is fully developed with a maximal Reynolds number of 1800, and thus is laminar.

A schematic of the experimental facility used in this study is shown in Fig. 2. Air is supplied from a 6 bar air supply passing through a pressure regulator, two consecutive particle filters and a moisture filter. After the filters, a mass flow control unit (BROOKS Smart Mass Flow) is connected and used to control the flow rate that is passing through the channels. Pressure drop measurements were taken 1 mm before and after the sample using a differential pressure sensor (Honeywell 24 PCE sensor). The pressure sensor is carefully calibrated by referencing it to a Pneumatic Intelligent Pressure Scanner (Model 9116). The pressure measurement is used to study the influence of the sample surface on characteristics of the flow. The friction factor for the sample between the two pressure ports is:

$$f = \frac{\Delta P}{\frac{1}{D_h}\frac{\rho_f \cdot \bar{u}^2}{2}} \tag{2}$$

The Reynold number of the flow inside the rectangular channel is given as:

$$Re_{Dh} = \frac{\rho_f \cdot \bar{u} \cdot D_h}{\mu_f} \tag{3}$$

The flow inlet temperature is measured before the inlet of the micro-channel setup using a T-type thermocouple. The Pt thin film layer, deposited on the back of the each sample, has a dual purpose; it is used to heat the sample and to measure the average temperature of the silicon chip. The temperature of the sample is obtained using the resistance of the thin film Pt layer, which is a known function of temperature. The thermal coefficient of resistance (TCR) of the thin film Pt layer was measured in the range 16–95 °C and was found to be ~0.00351/°C. The voltage output due to the resistance of the thin film Pt heater and the shunt are measured using a National Instrument data logger (NI-PCI-6280 module). Using Labview, the measured voltage and current are directly translated into resistance and temperature measurements.

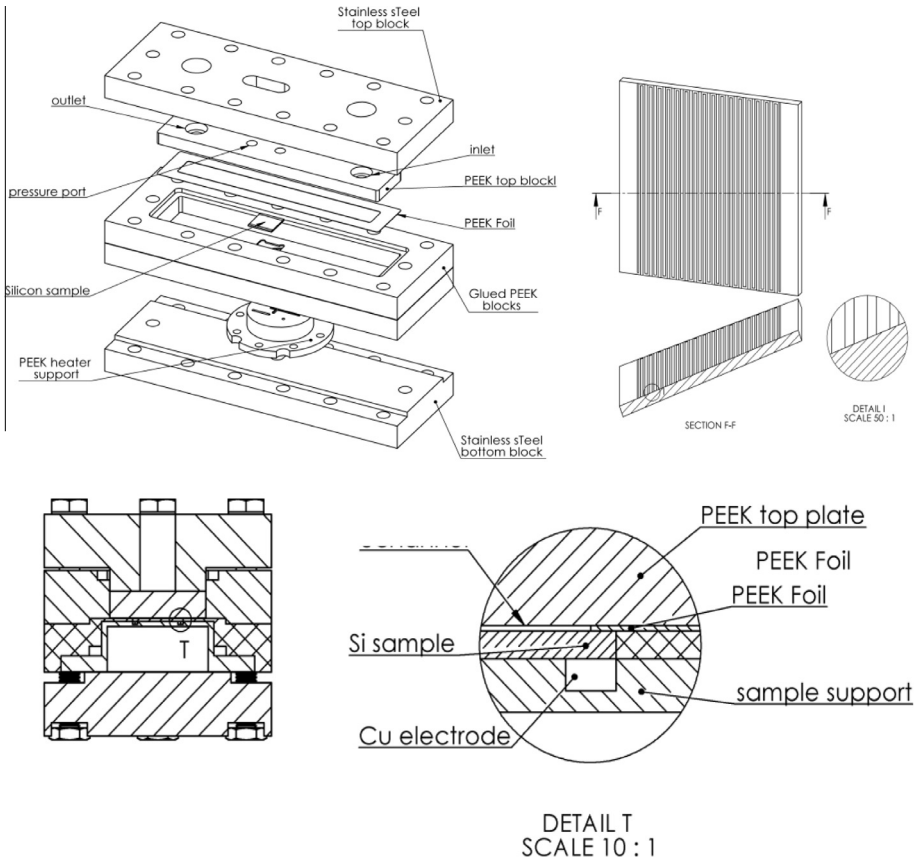

Fig. 1. Detailed view of rectangular micro-channel set-up.

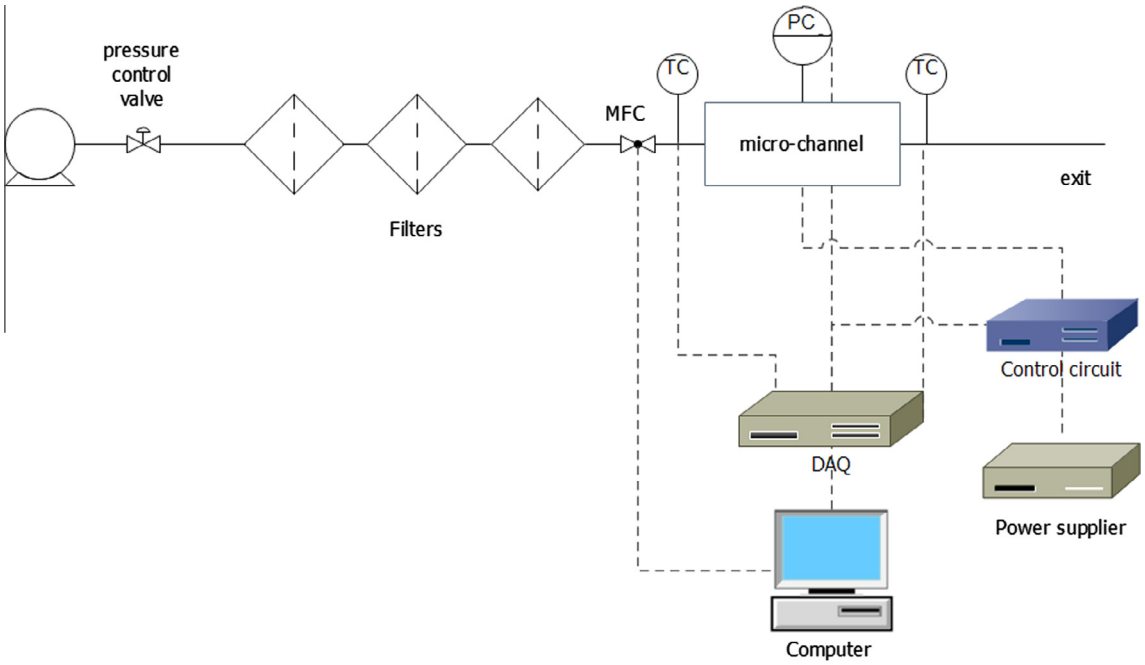

Fig. 2. Schematic of the experimental setup flow and control loop.

During the heat transfer experiments, the set temperature of the sample is controlled by controlling the power supplied to the sample.

The log mean temperature difference can be considered as the driving force for the heat transfer from the sample to the surrounding flowing fluid, and it is described as:

$$\Delta T_{LMTD} = \frac{T_2 - T_1}{ln\left(\frac{T_s - T_1}{T_s - T_2}\right)} \quad (4)$$

The sample exit temperature is calculated as:

$$T_2 = \frac{V \cdot i}{\dot{m} \cdot Cp_f} + T_1 \quad (5)$$

The average heat transfer coefficient of the sample is defined as:

$$h = \frac{V \cdot i}{A \cdot \Delta T_{LMTD}} \quad (6)$$

The average Nusselt number is calculated as:

$$\overline{Nu}_{Dh} = \frac{h \cdot D_h}{k_f} \quad (7)$$

The heat transfer and pressure drop of the various samples inside the rectangular channel are evaluated by comparing the results with results of pressure drop and Nusselt number of the fully developed laminar flow in a bare micro-channel. The evaluation of the Nusselt number for the modified sample is made by assuming worst case scenario where the CNTs layer is impermeable to the flow, thus reducing the hydraulic diameter of the channel. The heat transfer enhancement and their respective pressure drop penalty are defined as:

$$\eta_T = \left[\frac{\overline{Nu}_{Dh}^{CNTs}}{\overline{Nu}_{Dh}^{Bare}}\right] \quad (8)$$

$$\eta_p = \left[\frac{\Delta P_{CNTs}}{\Delta P_{bare}}\right] \quad (9)$$

The errors of the pressure drop and Nusselt numbers come from the random errors, instrumentation errors, and calibration errors. By performing a simple sequential perturbation error analysis, the maximum combined errors for Δp and Nu are less than 4.53% and 3.51% respectively.

2.2.1. Setup operating parameter

Despite a large number of publications regarding flow and heat transfer in microchannels, a large spread in results can be found. A bibliographical review made by Morini et al. [43] suggested that the correlations proposed by different authors, to predict the friction factor and Nusselt number inside micro-channels, are based on few experimental points with no theoretical background. Similarly, Asadi et al. [44] show large discrepancies between analytical and experimental data. Morini et al. [45] critically reviewed the measurement technique for analyzing the micro-flows and pointed out that the discrepancies of the available literature data originated from the experimental methods used. Following Morini et al. [43], this section focuses on pointing out the possible scaling effects which could influence the setup behavior. Table 1 summarizes the list of the major scaling effects, which are considered during the current study together with a selected number of significant references, and their corresponding threshold values for the rectangular micro-channels used.

Table 1
Major scaling factors, associated dimensionless number and threshold value.

Scaling effect	Dimensionless parameter	Negligible if:
Fluid axial conduction [46]	$Pe = Re \cdot Pr$	$\frac{50}{Pe} < 1$ [47]
Entrance effect [48,49]	$Gz = Re \cdot Pr \cdot \left(\frac{D_h}{l}\right)$	$\frac{Gz}{10} < 1$ [47]
Flow compressibility [48,50]	$Ma = \frac{u}{\sqrt{\gamma R T_f}}$	$\frac{Ma}{0.3} < 1$ [47,51]
Wall-fluid conjugate heat transfer [52–54]	$\lambda = \frac{k_w A_c}{\dot{m} \cdot Cp \cdot l}$	$\frac{\lambda}{0.01} < 1$ [47]
Viscous dissipation [48,55]	$Br_T = \frac{\mu_f u^2}{k_f (T_s - T_1)}$	$\frac{Br}{0.005} < 1$ [47]
Relative surface roughness [56,57]	$\epsilon = \frac{Sq}{D_h}$	$\frac{\epsilon}{0.05} < 1$ [47]

The different scaling effects such as the entrance effect, compressibility, viscous dissipation wall-fluid conjugated heat transfer, fluid axial conduction and surface roughness can significantly influence the measurements of both heat transfer and pressure drop. Since two channel heights (125 μm and 200 μm) are used to investigate the heat transfer performance of structured surfaces, the setup operating condition should be carefully selected in order to account the scaling effect that plays a significant role in determining the heat transfer and pressure drop measurements. This helps in determining the appropriate setup operating ranges which allows fair comparison of the measurement done by the two different channel sizes. This can be avoided by either determining operating conditions free of any scaling effects or having similar scaling effects with relatively the same magnitudes. The operating ranges of the dimensionless parameters linked to the various effects are calculated based on the operating conditions set for the experiments.

Fig. 3 shows the normalized dimensionless quantities related to scaling effects *versus* Reynold number. When the value of the normalized dimensionless value is less than unity, the corresponding scaling effect can be considered negligible. Fluid axial conduction and surface roughness are negligible for both channels. However, the entrance effect, conjugation heat transfer, compressibility and viscous dissipation are not negligible for two channel heights on the laminar flow regime. The lower operating range for the H = 125 μm channel is decided by the conjugation heat transfer effect which is Re = 800, the higher operating range is decided by flow compressibility scaling effect at Re = 1600. Similarly, the lower operating range for the H = 200 μm channel obtained is Re = 800 which is set by conjugated scaling effects, and the higher operating range is at Re = 2300, which is used to avoid the flow turbulence effect. However, viscous dissipation and entrance effect will continue to influence through a wide range of operating conditions. This might result a smaller discrepancy on the heat transfer measurement between the different sized microchannels. Based on this analysis of the possible scaling effects, the operating range for the rectangular microchannel is 800 < Re < 1600 which also satisfies fully developed laminar flow conditions.

2.3. Sample characterization

High resolution scanning electron-microscopy (Zeiss MERLIN HR-SEM) is used to obtain information of the surface morphology of the samples. Prior to the measurement samples are broken into two in order to study the cross-section of the synthesized layer. The internal structure of CNT's, i.e. the orientation if the graphene layers, was observed using high resolution transmission electron microscopy (HRTEM; Philips CM300ST-FEG equipped with Gatan Ultrascan 1000 CCD camera). This measurement is performed by removing the layer of carbon structures and collecting CNTs in the sample holder. The surface characteristics of each individual sample were studied using confocal microscopy (Laser scanning microscope VK 9700 Keyence), which enables to suppress all structural data outside the focal plane. This method helps to take data in each optical section and further reconstruct a 3D image of the surface with up to 18,000× magnification, spatial resolution of 120 nm and z-axis resolution of 1 nm. This allows measuring the surface profile, surface roughness and surface area by providing height data.

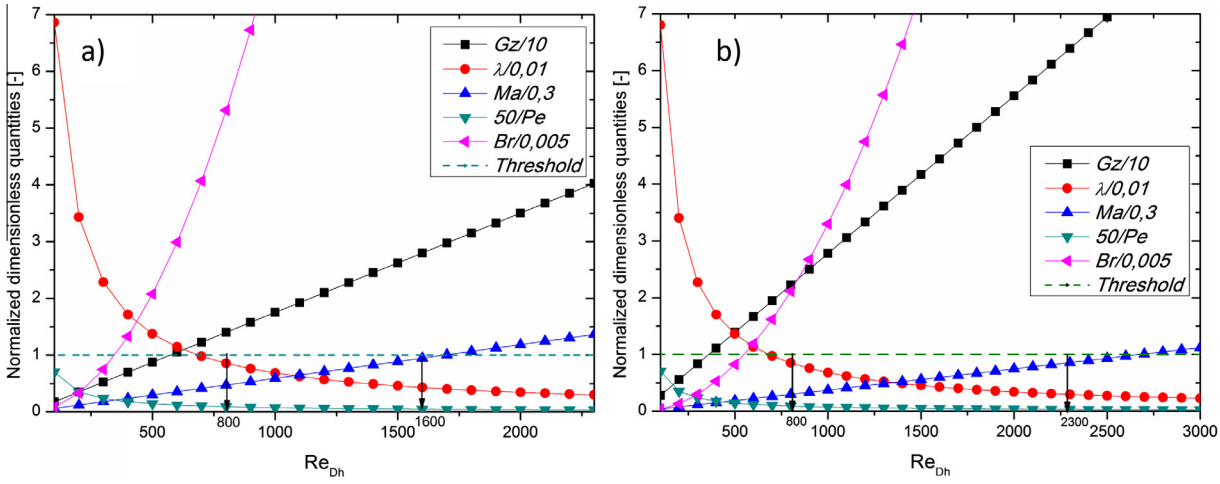

Fig. 3. Graphical representation of normalized dimensionless quantities related to scaling effects of a rectangular micro-channel with (a) $H = 125$ μm and (b) $H = 200$ μm.

3. Results and discussion

3.1. MWCNTs synthesis and characterization

Prior to the synthesis process, the thin film layer composed of 10 nm of Ta and 5 nm of Fe was reduced using H_2 during the heating of the reactor from ambient to 720 °C at a rate of 10 °C/min. The sample is further reduced for 1.8 h while maintaining the reactor temperature to 720 °C. This process results in de-wetting of the thin Fe film. Initially the possible oxide layer that exists on the thin film reduces to pure metal. This is followed by the rearrangement of the 5 nm Fe thin film into clusters of nanoparticles. Finally, the nanoparticles re-arrange themselves to a crystallographic orientation, which is favored by surface- and interface energy minimization or by strain energy density minimization [58]. Ng et al. [59] studied the growth of CNTs on various metal under layers using a highly efficient combinatorial approach. They noted that Ta and Al create a broader range of diameters. Similar results were obtained after the pretreatment of the Fe/Ta layer. Wang et al. [60] reported that the Ta adhesive layer helped the formation of the Fe nanoparticles with a hemispherical shape and high adhesion energy. Fig. 4 shows strong attachment of Fe nano-particles formation after the pretreatment process on substrate material. Using confocal microscopy, resulting in height data, the average size of the Fe particles was determined to be 109 nm with a maximum size of 280 nm.

After the treatment process, a controlled synthesis of a highly porous layer of CNTs was successfully achieved, see Fig. 5. By varying the synthesis period, the layer thickness of the CNTs was controlled. Two different thicknesses were obtained when exposing the reduced sample to the reacting hydrocarbon environment during different times. Samples exposed for 45 min possess an average layer thickness of 6 μm, while an exposure of 90 min resulted in a 20 μm thick layer of CNTs. Vertically alignment of the layers was achieved during the synthesis process. Wang et al. [60] reported that high surface tension materials such as Ta can promote vertically aligned dense CNTs grown on a metal supporting layer. The alignment is as a result of closely spaced catalyst nano particles self-assembled into rigid bundle layer due to the strong van der Waals interaction between the crowding nanotube[61]. For each sample, the average diameter of the CNTs was estimated based on 50 observations by post processing the SEM images using image processing software ImageJ. The average diameter of the CNTs synthesized for a period of 45 min and 90 min are 35 nm and 32 nm respectively. The smaller the average diameter creates a relatively denser morphology, see Fig. 5b and d.

In order to determine the surface characteristics of each sample such as surface roughness and external surface area, a thorough investigation of the sample surfaces was made by using the data obtained by confocal microscopy. Samples were scanned point by point from a selected depth (optical sectioning) and a 3D topology of the CNFs sample is reconstructed using the data with the inbuilt

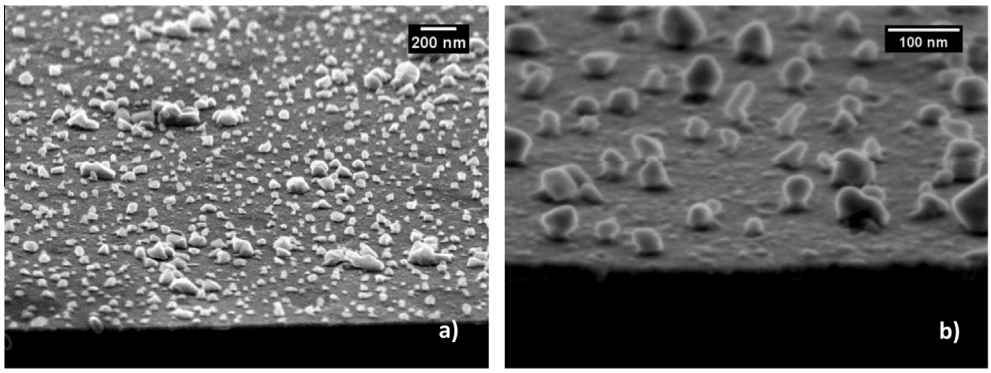

Fig. 4. Nano-particles on the surface after pretreatment of the 5 nm Fe/10 nm Ta thin film on silicon support by increasing the temperature from ambient to 720 °C at a rate of 10 °C/min and maintaining the temperature for 1.8 h.

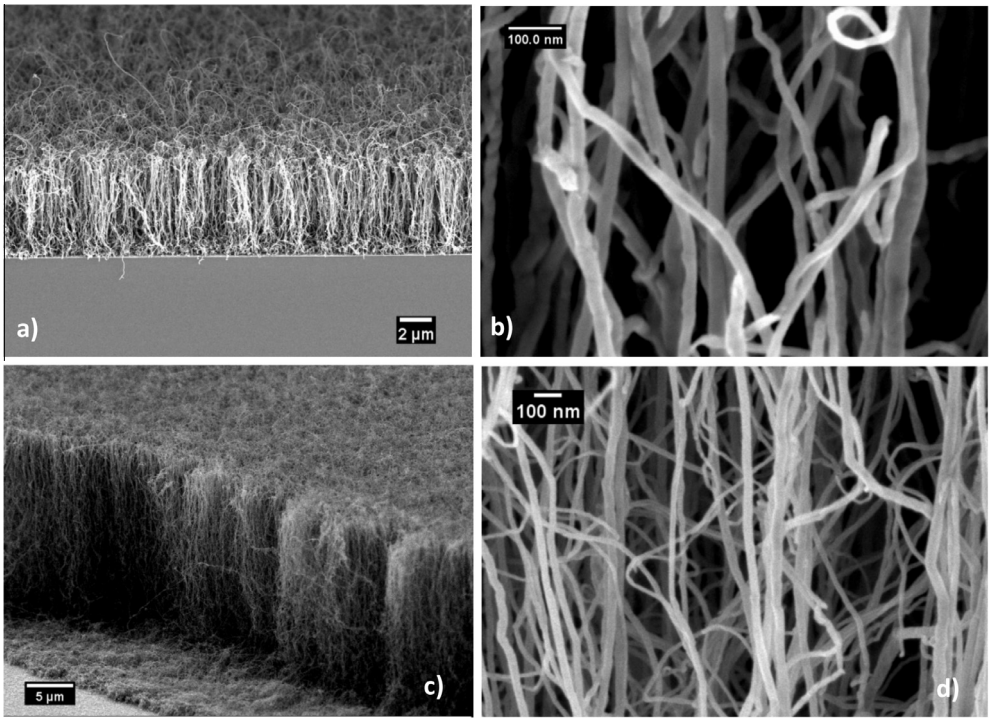

Fig. 5. SEM images of the deposited layer of two thick layer of MWCNTs (a, b) 6 μm thick layer with synthesis duration of 45 min and (c, d) 20 μm thick layer with synthesis duration of 90 min.

computer program (VK analyzer). The existing noise is eliminated using a Gaussian image filtering technique, which averages the entire image while leaving more of the sample's features. The structural variation of the surface is measured, evaluated and compared to the bare sample. The average and root mean square (RMS) surface roughness of each sample is calculated as:

$$S_a = \frac{1}{N} \cdot \sum_{i=0}^{N} |Z_i - \bar{Z}| \tag{10}$$

$$S_q = \sqrt{\frac{1}{N} \cdot \sum_{i=0}^{N} (Z_i - \bar{Z})^2} \tag{11}$$

The data was processed to obtain surface information such as surface roughness and external surface area. For both samples a similar structure of the surface was expected, because only the synthesis period was different. However, the mean and root-mean-square surface roughness of the sample synthesized at 45 min and 90 min were found to be (S_a = 1.062 μm, S_q = 1.333 μm) and (S_a = 0.717 μm, S_q = 0.954 μm) respectively. The difference of surface roughness data between the two samples is attributed to the fiber layer thickness. Large enhancement of the external surface area was achieved for both samples. The external surface area ratio between the surfaces produced compared to the projected area of the sample is 7 and 7.1 times, for 45 min and 90 min synthesis period respectively.

Fig. 6 shows the high resolution transmission electron microscopy (HRTEM) of individual nanofibers. A tubular structure is observed for each nanofibers which is made up of multiple layer of graphene sheet. Fig. 6b shows the Fast Fourier Transform (FFT) of the selected area (white rectangle) is plotted in the right corner of the HRTEM image. The stacking direction of the graphene sheets can be determined by using the FFT result, which is perpendicular to the direction of the line drawn from point 1–2. As a result, the basal planes of the graphene layer are parallel to the axis of the nanotube. The distance between the atomic layers, determined by post-processing the FFT image, of the graphene layer was found to be a(MWCNTs) = 0.35 nm which is comparable to a(graphite) = 3.35 nm [62]. The FFT of the HRTEM can also be used to determine crystallinity of the multiwalled nanotube. Lehman et al. [63] showed that the extent of crystallinity can be established by the FFT of HRTEM image of a MWCNT, provided that the HRTEM is highly focused. It was suggested that if the FFT consists of narrow sharp spots, as shown in Fig. 6b, the material is highly crystalline. However, if the material has blurred and wider spot, the material is less crystalline. The room temperature thermal conductivity of the graphene layer along the *a*-axis (in-plane) is greater than 3000 W/m K [64] while the conductivity along the *c*-axis (out-of-plane) can be as poor as 1.52 W/m K [65]. As a result, the thermal conductivity of the MWCNT is highly anisotropic. This influences the effective thermal conductivity of the individual strand of fibers. Moreover, the degree of crystallinity, crystallite shape, crystallite size, and presence of impurities has strong influence on the thermal conductivity of the fibers. However, quantitative measurement of thermal transport properties of individual fibers remains challenging, due to technological difficulties associated with nano-scale experimental measurements [66].

Wang et al. [60] in their model suggested that Fe nanoparticles deposited in a Ta layer leads to fast synthesis of CNT growth, which proceeds according to the base growth mode. However, in the current study, contradicting results were obtained during the synthesis of the CNTs. Fig. 6d shows the existence of the nanoparticles at the tip and within the CNTs. This provides an evidence of the existence of all possible growth mechanisms.

3.2. Heat transfer performance

In this section, the heat transfer performances for both bare and structured samples are experimentally evaluated in a hydrodynamically fully developed rectangular laminar channel flow. The influence of the CNTs on the heat transfer and pressure drop

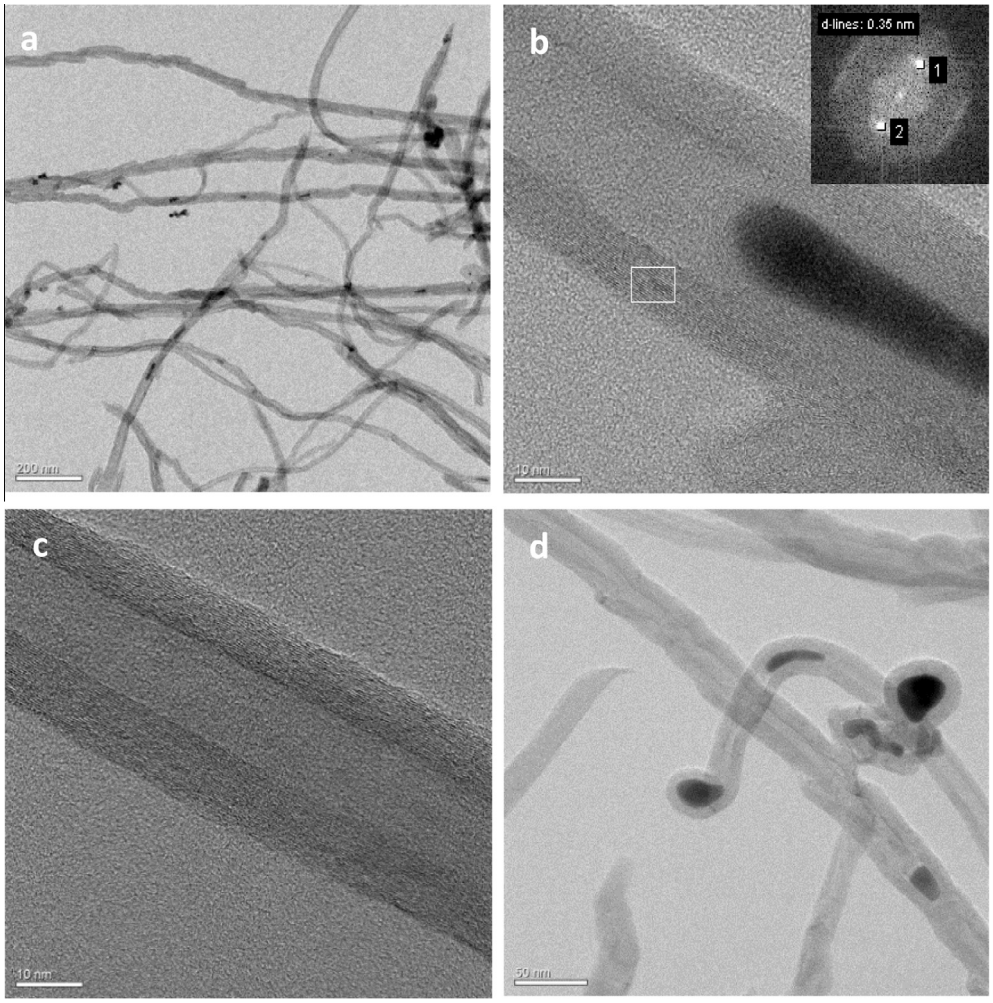

Fig. 6. HRTEM images of MWCNTs. (a, d) Fe nanoparticles inside and at the tip of the fibers. (b, c) Graphene layer orientation leading to multiwalled CNTs. In the top right corner of figures b result of FFT's are shown.

is investigated by comparing the structured samples with the bare silicon samples.

For the bare channels, the experimentally obtained pressure drop results show good agreement with the predicted conventional theory with data deviations, ±4.2% for $H = 125$ μm and ±3.8% for $H = 200$ μm, see Fig. 7. This is due to the relative surface roughness (<5%) for both channel sizes, which is negligible. Similar results were reported for liquids [67–69] and gases [70,71] in rectangular micro-channels, which agrees with conventional theory. The pressure drop obtained for the bare silicon sample are used as a bench mark to compare the flow characteristics of the samples covered with CNTs. Fig. 7 shows an increase in pressure drop with

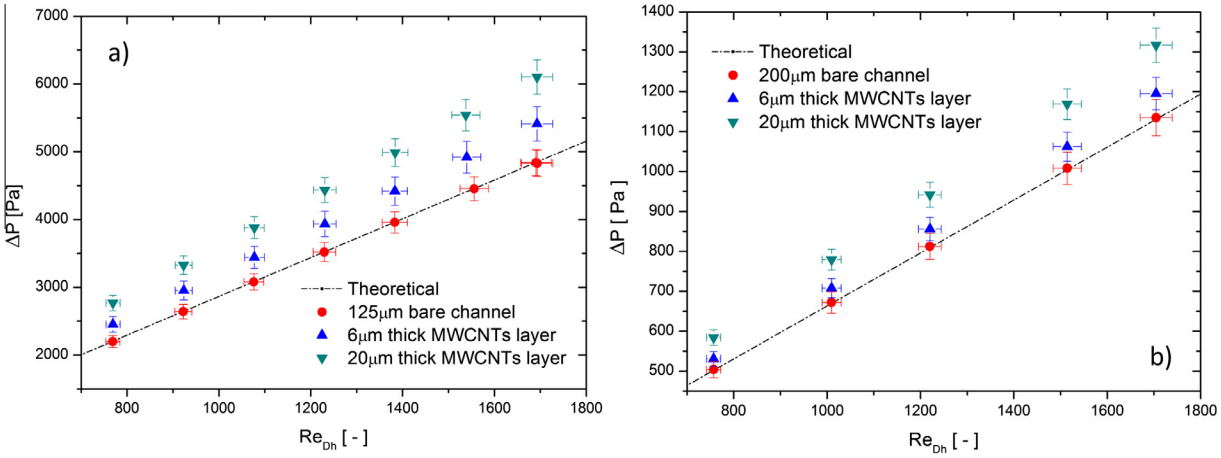

Fig. 7. Pressure drop as a function of Reynold number for each samples inside (a) $H = 125$ μm and (b) $H = 200$ μm height rectangular microchannel.

respect to the CNTs layer height for both channel sizes. For the 125 μm channel height, the 6 and 20 μm thick layer of CNTs resulted in 12% and 26% increase in pressure drop respectively. Pressure drop results obtained for the 200 μm channel height show a similar trend with an increase of 6% and 16.4% for 6 and 20 μm CNTs layer thickness respectively.

The friction factor of microchannel flow is generally affected by the channel surface conditions such as roughness height, spacing, shape and type. And for the same hydraulic diameter, the friction factors are also dependent on the geometrical configuration of the microchannel such as shape and aspect ratio. The theoretical friction factor of the microchannel is represented as:

$$f_{theoretical} = \frac{W^2 + H^2}{(W+H)^2} \cdot \frac{24}{Re_{Dh}} \tag{12}$$

The relative surface roughness of the CNTs layers inside both channel heights is significantly less than 5%, see Table 2. As a result, the influence of surface roughness on the friction factor can be considered negligible. However, the CNTs layers result in decreasing the flow cross-section with less flow passing through the flow resisting CNTs layer and accelerating flow above the layer. This results in constricting the hydraulic diameter of the channel which resulted in an increase in pressure drop. The friction factor calculated based on the constricted flow hydraulic diameter has a very small deviation when it is compared to the theoretical friction factor value, see Fig. 8. This is in agreement with Kandlikar et al. [72,73]. Therefore, the reduction of the channel height, due to the deposited CNT layer, is the main reason behind the increase in pressure drop.

Prior to the heat transfer to the nanostructured surfaces, the heat transfer characteristics of the rectangular microchannels were studied. The systematically chosen operating flow range for the rectangular microchannel partially reduces the influence of the scaling factors. The entrance effect and viscous dissipation, however, play a significant role in shaping the heat transfer behavior of the samples. Fig. 9 shows the heat transfer performance of each sample with and without nanostructured surfaces with their corresponding channel height. An increasing trend of the Nusselt number with Reynold number can be seen for both channel heights. This is mainly attributed to the thermal entrance effect resulting in a thermally developing flow. Moreover, the entrance effect results in higher Nusselt number compared to a thermally developed flow. In contrast, it can be seen that the Nusselt number of the 125 μm height channel is slightly lower than the 200 μm height. This is solely attributed to the viscous dissipation which increases with a decrease in hydraulic diameter.

The vertically aligned MWCNTs layers successfully enhance the heat transfer performance of the sample inside the rectangular micro-channels, see Fig. 9. An average heat transfer enhancement of 19% and 74% is obtained inside the 125 μm height microchannel with 6 μm and 20 μm CNTs layer thickness respectively. Whereas, the average heat transfer enhancement of 22% and 62% are obtained inside the 200 μm channel with corresponding CNTs layer thicknesses of 6 μm and 20 μm. Since the nanostructured layer composed of highly porous strands of MWCNTs, the method of enhancement are separately studied by reviewing the structural characteristics of the samples. Table 2 summarizes the structural morphology of the samples. The relative surface roughness of both samples is less than 1% which results in negligible influence in heat transfer, see Table 1. The samples exhibit comparable improved external surface areas ratio. This surface area can increase the heat transfer only if the layer exhibits extremely low porosity, which will results in a highly conductive CNT layer. This hypothetical conductive layer will result in negligible thermal resistance while increasing the surface area. However, this enhancement method is overruled due to the extremely high porosity of the layer.

The CNTs layer exhibit extremely high internal surface area which is highly dependent on the height of the layer. The extremely high porosity of the CNTs can insure heat transfer only with partially or fully flow permeable layer. When the flowing fluid is fully or partially penetrates through the porous CNTs layer, the

Table 2
Summary of structural morphology of the vertically aligned MWCNTs layers.

Samples	Layer thickness (avg.)	Fiber dia. (avg)	Ex. surface area ratio [–]	Surface roughness [μm]	
				S_a	S_q
Sample 1 (45 min)	6 μm	35 nm	~7	1.062	1.333
Sample 2 (90 min)	20 μm	32 nm	~7.1	0.717	0.954

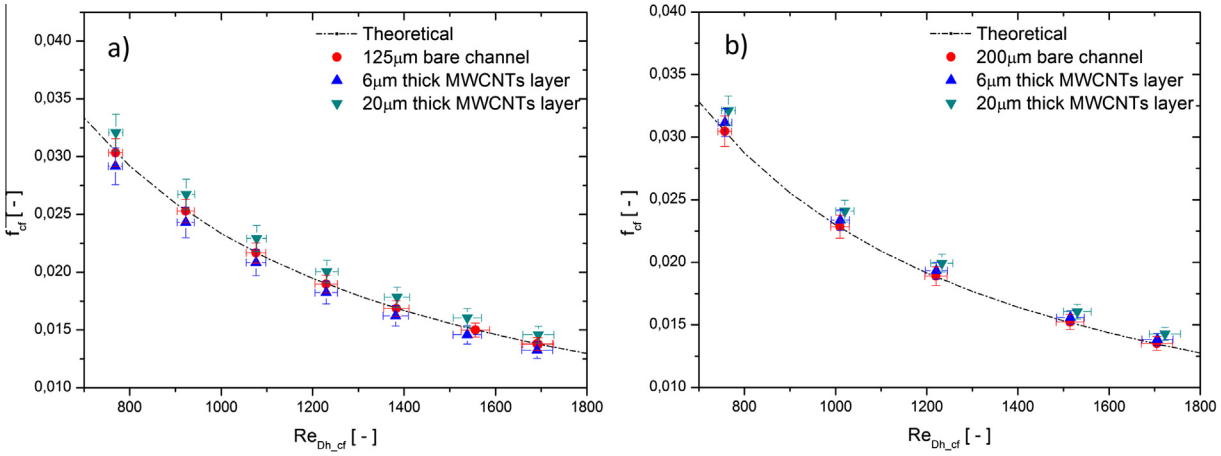

Fig. 8. Friction factor as a function of Reynold number using the constricted flow hydraulic diameter for all samples inside (a) H = 125 μm and (b) H = 200 μm.

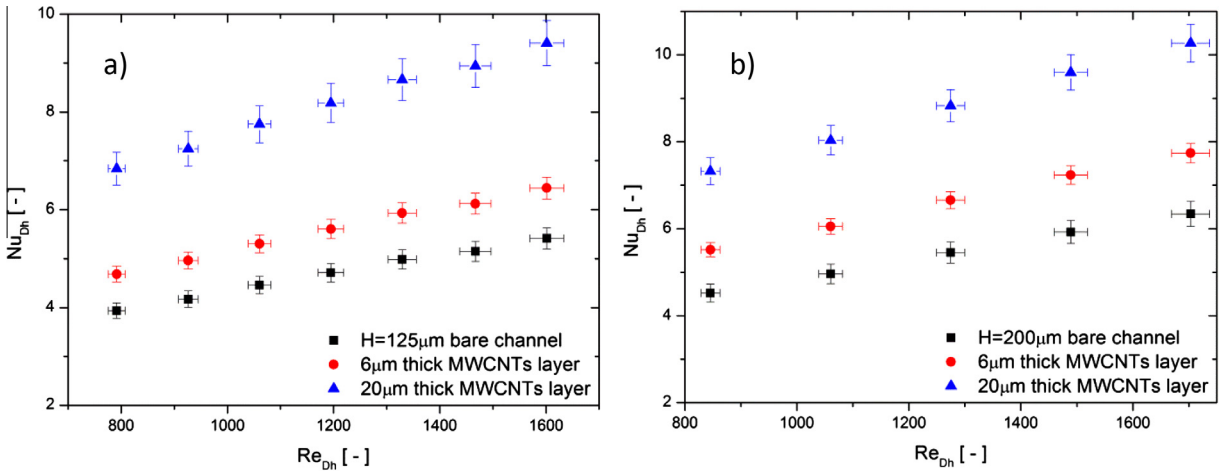

Fig. 9. Heat transfer measurement of the bare silicon sample in rectangular microchannel with (a) $H = 125$ μm and (b) $H = 200$ μm.

effective thermal conductivity inside the thermal boundary layer increases, hence lower thermal resistance. As a result, the thermal resistance of the sample with 20 μm layer thickness is significantly lower than 6 μm thick sample.

Different heat transfer and pressure drop results were obtained for the same samples under different channel height. Fig. 10 shows the average enhancement heat transfer and pressure drop for each measurement with respect to the CNTs layer thickness ratio $\left(\frac{h_{CNT}}{D_h}\right)$. The result shows an increase in pressure drop with an increase of the CNTs layer thickness ratio. This is attributed to the flow restriction created by the deposited layer of CNTs. In contrast, an increasing trend in heat transfer can only be guaranteed for samples measured with the same channel height. For instance, for smaller difference in height ratio, even though the samples tested exhibit exactly similar layer morphology and topology, lower heat transfer performance was obtained for the channel height of 125 μm compared to 200 μm, see Fig. 10. This is mainly attributed to the scaling effect induced by the structured surface which increases the local viscous dissipation. The local viscous dissipation competes with heat transfer resulting in lower heat transfer enhancement compared to the bigger channel size.

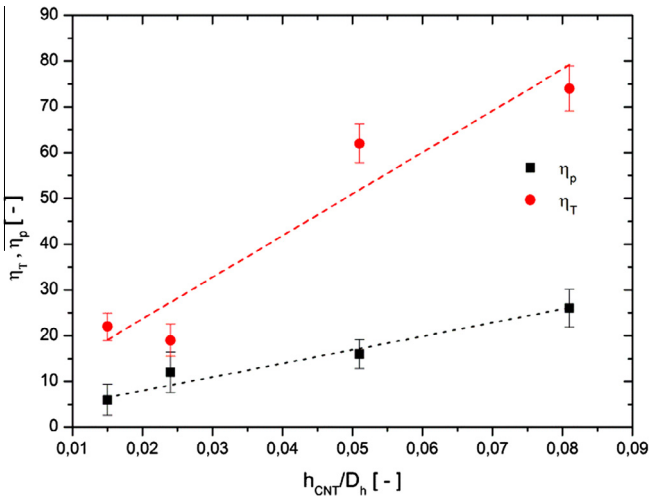

Fig. 10. Overall heat transfers and pressure drop enhancement compared to the relative CNTs layer height.

4. Conclusion and recommendation

The present study brings about the convective heat transfer behavior of different layer thicknesses of CNTs deposited on a silicon substrate in a rectangular microchannel. Using a catalytic vapor deposition process, a successful synthesis of vertically aligned MWCNTs was obtained. By varying the synthesis period, two different thicknesses of CNT layers, with 6 μm and 20 μm layer thicknesses, were made. A thorough morphological and topological characterization of the samples was made. An experimental approach is used to compare the heat transfer performance of the CNT deposited samples with the bare silicon samples. The experimental results show that the pressure drop of the highly porous CNT layer increases with an increase of CNTs layer thickness. A significant heat transfer enhancement was obtained by enhancing the heat transfer surface using a layer of CNTs. It was demonstrated that the heat transfer enhancement is highly dependent on the thickness of the CNTs layer, resulting higher effective thermal conductivity inside the thermal boundary layer. Moreover, the heat transfer results indicated that the enhancement potential of the samples can be compromised with the scaling effects, especially viscous dissipation. Further investigation is needed to point out the competing effect of the scaling effects in reducing the heat transfer enhancement.

Acknowledgment

We acknowledge financial support for this research from ADEM, A green Deal in Energy Materials of the Ministry of Economic Affairs of The Netherlands (http://www.adem-innovationlab.nl).

References

[1] J. Darabi, K. Ekula, Development of a chip-integrated micro cooling device, Microelectron. J. 34 (11) (2003) 1067–1074, http://dx.doi.org/10.1016/j.mejo.2003.09.010.
[2] D.A. Van Den Ende, H.J. Van De Wiel, R.H.L. Kusters, A. Sridhar, J.F.M. Schram, M. Cauwe, J. Van Den Brand, Mechanical and electrical properties of ultra-thin chips and flexible electronics assemblies during bending, Microelectron. Reliab. 54 (12) (2014) 2860–2870, http://dx.doi.org/10.1016/j.microrel.2014.07.125.
[3] J.J. Yu, C.A. Yang, Y.F. Lin, C.H. Hsueh, C.R. Kao, Optimal Ag addition for the elimination of voids in Ni/SnAg/Ni micro joints for 3D IC applications, J. Alloys Compd. 629 (2015) 16–21, http://dx.doi.org/10.1016/j.jallcom.2015.01.001.
[4] S.K. Yoo, J.H. Lee, S.-S. Yun, M.B. Gu, J.H. Lee, Fabrication of a bio-mems based cell-chip for toxicity monitoring, Biosens. Bioelectron. 22 (8) (2007) 1586–1592, http://dx.doi.org/10.1016/j.bios.2006.07.014.
[5] X. Chen, D. Cui, C. Liu, H. Cai, Fabrication of solid phase extraction DNA chips based on bio-micro-electron-mechanical system technology, Chin. J. Anal.

Chem. 34 (3) (2006) 433–437, http://dx.doi.org/10.1016/S1872-2040(06)60022-4.
[6] I. Byun, J. Yang, S. Park, Fabrication of a new micro bio chip and flow cell cytometry system using bio-mems technology, Microelectron. J. 39 (5) (2008) 717–722, http://dx.doi.org/10.1016/j.mejo.2007.12.004.
[7] L.P. Wang, P.G. Shao, J.A. Van Kan, A.A. Bettiol, F. Watt, Development of elastomeric lab-on-a-chip devices through proton beam writing (Pbw) based fabrication strategies, Nucl. Instrum. Methods Phys. Res., Sect. B 267 (12–13) (2009) 2312–2316, http://dx.doi.org/10.1016/j.nimb.2009.03.044.
[8] N.-T. Nguyen, S.a.M. Shaegh, N. Kashaninejad, D.-T. Phan, Design, fabrication and characterization of drug delivery systems based on lab-on-a-chip technology, Adv. Drug Deliv. Rev. 65 (11–12) (2013) 1403–1419, http://dx.doi.org/10.1016/j.addr.2013.05.008.
[9] B.-K. Lee, J.M. Park, D.S. Kim, T.H. Kwon, A Simple fabrication and integration technique of microlens for microfluidic lab-on-a-chip by overflow of UV resin through holes, Curr. Appl. Phys. 11 (3) (2011) 909–913, http://dx.doi.org/10.1016/j.cap.2010.12.021.
[10] A.E. Guber, M. Heckele, D. Herrmann, A. Muslija, V. Saile, L. Eichhorn, T. Gietzelt, W. Hoffmann, P.C. Hauser, J. Tanyanyiwa, A. Gerlach, N. Gottschlich, G. Knebel, Microfluidic lab-on-a-chip systems based on polymers—fabrication and application, Chem. Eng. J. 101 (1–3) (2004) 447–453, http://dx.doi.org/10.1016/j.cej.2004.01.016.
[11] T. Suzuki, Y. Funahashi, T. Yamaguchi, Y. Fujishiro, M. Awano, Fabrication and characterization of micro tubular SOFCs for advanced ceramic reactors, J. Alloys Compd. 451 (1–2) (2008) 632–635, http://dx.doi.org/10.1016/j.jallcom.2007.04.149.
[12] B. Jiang, T. Maeder, A.J. Santis-Alvarez, D. Poulikakos, P. Muralt, A low-temperature co-fired ceramic micro-reactor system for high-efficiency on-site hydrogen production, J. Power Sources 273 (2015) 1202–1217, http://dx.doi.org/10.1016/j.jpowsour.2014.09.084.
[13] H.C. Foo, N.W. Smith, S.M.R. Stanley, Fabrication of an on-line enzyme micro-reactor coupled to liquid chromatography-tandem mass spectrometry for the digestion of recombinant human erythropoietin, Talanta 135 (2015) 18–22, http://dx.doi.org/10.1016/j.talanta.2014.12.033.
[14] R.W. Verjulio, J. Santander, N. Sabaté, J.P. Esquivel, N. Torres-Herrero, A. Habrioux, N. Alonso-Vante, Fabrication and evaluation of a passive alkaline membrane micro direct methanol fuel cell, Int. J. Hydrogen Energy 39 (10) (2014) 5406–5413, http://dx.doi.org/10.1016/j.ijhydene.2013.12.014.
[15] A. Omosebi, R.S. Besser, Fabrication and performance evaluation of an in-membrane micro-fuel cell, J. Power Sources 242 (2013) 672–676, http://dx.doi.org/10.1016/j.jpowsour.2013.05.140.
[16] S.-S. Hsieh, C.-F. Huang, Design, fabrication and performance test of a planar array module-type micro fuel cell stack, Energy Convers. Manage. 76 (2013) 971–979, http://dx.doi.org/10.1016/j.enconman.2013.08.062.
[17] J.A. Alanís-Navarro, C. Reyes-Betanzo, J. Moreira, P.J. Sebastian, Fabrication and characterization of a micro-fuel cell made of metallized PMMA, J. Power Sources 242 (2013) 1–6, http://dx.doi.org/10.1016/j.jpowsour.2013.05.048.
[18] J. Fernández, R. Poulter, Radial mass flow in electrohydrodynamically-enhanced forced heat transfer in tubes, Int. J. Heat Mass Transfer 30 (10) (1987) 2125–2136, http://dx.doi.org/10.1016/0017-9310(87)90091-3.
[19] M.K. Bologa, I.K. Savin, A.B. Didkovsky, Electric-field-induced enhancement of vapour condensation heat transfer in the presence of a non-condensable gas, Int. J. Heat Mass Transfer 30 (8) (1987) 1577–1585, http://dx.doi.org/10.1016/0017-9310(87)90302-4.
[20] J.W. Zhou, Y.G. Wang, G. Middelberg, H. Herwig, Unsteady jet impingement: heat transfer on smooth and non-smooth surfaces, Int. Commun. Heat Mass Transfer 36 (2) (2009) 103–110, http://dx.doi.org/10.1016/j.icheatmasstransfer.2008.10.020.
[21] P. Xu, B. Yu, S. Qiu, H.J. Poh, A.S. Mujumdar, Turbulent impinging jet heat transfer enhancement due to intermittent pulsation, Int. J. Therm. Sci. 49 (7) (2010) 1247–1252, http://dx.doi.org/10.1016/j.ijthermalsci.2010.01.020.
[22] N. Khan, D. Pinjala, K.C. Toh, Pool Boiling Heat Transfer Enhancement by Surface Modification/Micro-Structures for Electronics Cooling: A Review, pp. 273–280, doi: 10.1109/EPTC.2004.1396618 (2004).
[23] A. Miyara, Y. Otsubo, S. Ohtsuka, Y. Mizuta, Effects of fin shape on condensation in herringbone microfin tubes, Int. J. Refrig. 26 (4) (2003) 417–424, http://dx.doi.org/10.1016/S0140-7007(02)00154-8.
[24] L. Tadrist, M. Miscevic, O. Rahli, F. Topin, About the use of fibrous materials in compact heat exchangers, Exp. Thermal Fluid Sci. 28 (2–3) (2004) 193–199, http://dx.doi.org/10.1016/S0894-1777(03)00039-6.
[25] K. Boomsma, D. Poulikakos, F. Zwick, Metal foams as compact high performance heat exchangers, Mech. Mater. 35 (12) (2003) 1161–1176, http://dx.doi.org/10.1016/j.mechmat.2003.02.001.
[26] T.J. Lu, H.A. Stone, M.F. Ashby, Heat transfer in open-cell metal foams, Acta Mater. 46 (10) (1998) 3619–3635, http://dx.doi.org/10.1016/S1359-6454(98)00031-7.
[27] A. Ejlali, A. Ejlali, K. Hooman, H. Gurgenci, Application of high porosity metal foams as air-cooled heat exchangers to high heat load removal systems, Int. Commun. Heat Mass Transfer 36 (7) (2009) 674–679, http://dx.doi.org/10.1016/j.icheatmasstransfer.2009.03.001.
[28] M.-S. Liu, M. Ching-Cheng Lin, I.T. Huang, C.-C. Wang, Enhancement of thermal conductivity with carbon nanotube for nanofluids, Int. Commun. Heat Mass Transfer 32 (9) (2005) 1202–1210, http://dx.doi.org/10.1016/j.icheatmasstransfer.2005.05.005.
[29] K.-J. Park, D. Jung, Enhancement of nucleate boiling heat transfer using carbon nanotubes, Int. J. Heat Mass Transfer 50 (21–22) (2007) 4499–4502, http://dx.doi.org/10.1016/j.ijheatmasstransfer.2007.03.012.
[30] S. Launay, A.G. Fedorov, Y. Joshi, A. Cao, P.M. Ajayan, Hybrid micro-nano structured thermal interfaces for pool boiling heat transfer enhancement, Microelectron. J. 37 (11) (2006) 1158–1164, http://dx.doi.org/10.1016/j.mejo.2005.07.016.
[31] Z.-H. Liu, L. Liao, Forced convective flow and heat transfer characteristics of aqueous drag-reducing fluid with carbon nanotubes added, Int. J. Therm. Sci. 49 (12) (2010) 2331–2338, http://dx.doi.org/10.1016/j.ijthermalsci.2010.08.001.
[32] K. Kordás, G. Tóth, P. Moilanen, M. Kumpumäki, J. Vähäkangas, A. Uusimäki, R. Vajtai, P.M. Ajayan, Chip cooling with integrated carbon nanotube microfin architectures, Appl. Phys. Lett. 90 (12) (2007), http://dx.doi.org/10.1063/1.2714281.
[33] Z. Mo, R. Morjan, J. Anderson, E.E. Campbell, L. Johan, Integrated nanotube microcooler for microelectronics applications 1 (2005) 51–54, 10.1109/ECTC.2005.1441244.
[34] S. Shenoy, J.F. Tullius, Y. Bayazitoglu, Minichannels with carbon nanotube structured surfaces for cooling applications, Int. J. Heat Mass Transfer 54 (25–26) (2011) 5379–5385, http://dx.doi.org/10.1016/j.ijheatmasstransfer.2011.08.005.
[35] J.F. Tullius, Y. Bayazitoglu, Effect of Al_2O_3/H_2O nanofluid on MWNT circular fin structures in a minichannel, Int. J. Heat Mass Transfer 60 (2013) 523–530, http://dx.doi.org/10.1016/j.ijheatmasstransfer.2013.01.035.
[36] I. Tuzovskaya, S. Pacheco Benito, J.K. Chinthaginjala, C. Reed, L. Lefferts, T. Van Der Meer, Heat exchange performance of stainless steel and carbon foams modified with carbon nano fibers, Int. J. Heat Mass Transfer 55 (21–22) (2012) 5769–5776, http://dx.doi.org/10.1016/j.ijheatmasstransfer.2012.05.073.
[37] T.J. Taha, D.B. Thakur, T.H.V.D. Meer, Towards convective heat transfer enhancement: surface modification, characterization and measurement techniques, J. Phys: Conf. Ser. 395 (1) (2012) 012113, http://dx.doi.org/10.1088/1742-6596/395/1/012113.
[38] T.J. Taha, T.H. Van Der Meer, Influence of CNFS layer morphology on convective heat transfer behavior, 8th World Conference on Experimental Heat Transfer, Fluid Mechanics, and Thermodynamics, Lisbon, Portugal, 7 (2013).
[39] T.J. Taha, L. Lefferts, T.H. Van Der Meer, Indirect involvement of amorphous carbon layer on convective heat transfer enhancement using carbon nanofibers, J. Heat Transfer 137 (9) (2015), http://dx.doi.org/10.1115/1.4030218. pp. 091007-091007.
[40] A.V. Melechko, V.I. Merkulov, T.E. Mcknight, M.A. Guillorn, K.L. Klein, D.H. Lowndes, M.L. Simpson, Vertically aligned carbon nanofibers and related structures: controlled synthesis and directed assembly, J. Appl. Phys. 97 (4) (2005), http://dx.doi.org/10.1063/1.1857591.
[41] R.M. Tiggelaar, R.G.P. Sanders, A.W. Groenland, J.G.E. Gardeniers, Stability of thin platinum films implemented in high-temperature microdevices, Sens. Actuators, A 152 (1) (2009) 39–47, http://dx.doi.org/10.1016/j.sna.2009.03.017.
[42] D.B. Thakur, R.M. Tiggelaar, J.G.E. Gardeniers, L. Lefferts, K. Seshan, Growth of carbon nanofiber coatings on nickel thin films on fused silica by catalytic thermal chemical vapor deposition: on the use of titanium, titanium-tungsten and tantalum as adhesion layers, Surf. Coat. Technol. 203 (22) (2009) 3435–3441, http://dx.doi.org/10.1016/j.surfcoat.2009.05.011.
[43] G.L. Morini, Single-phase convective heat transfer in microchannels: a review of experimental results, Int. J. Therm. Sci. 43 (7) (2004) 631–651, http://dx.doi.org/10.1016/j.ijthermalsci.2004.01.003.
[44] M. Asadi, G. Xie, B. Sunden, A review of heat transfer and pressure drop characteristics of single and two-phase microchannels, Int. J. Heat Mass Transfer 79 (2014) 34–53, http://dx.doi.org/10.1016/j.ijheatmasstransfer.2014.07.090.
[45] G.L. Morini, Y. Yang, H. Chalabi, M. Lorenzini, A critical review of the measurement techniques for the analysis of gas microflows through microchannels, Exp. Thermal Fluid Sci. 35 (6) (2011) 849–865, http://dx.doi.org/10.1016/j.expthermflusci.2011.02.005.
[46] R.K. Shah, A.L. London, Laminar flow forced convection in ducts, Adv. Heat Transfer 14 (1978) 196–220.
[47] Y.Y. Morini Gian Luca, Guidelines for the determination of single-phase forced convection coefficients in microchannels, J. Heat Transfer 135 (10) (2013) 101004, http://dx.doi.org/10.1115/1.4024499. 10 p.
[48] Z.-Y. Guo, Z.-X. Li, Size effect on microscale single-phase flow and heat transfer, Int. J. Heat Mass Transfer 46 (1) (2003) 149–159, http://dx.doi.org/10.1016/S0017-9310(02)00209-0.
[49] C. Li, L. Jia, T. Zhang, The entrance effect on gases flow characteristics in microtube, J. Therm. Sci. 18 (4) (2009) 353–357, http://dx.doi.org/10.1007/s11630-009-0353-5.
[50] G.L. Morini, M. Lorenzini, S. Colin, S. Geoffroy, Experimental analysis of pressure drop and laminar to turbulent transition for gas flows in smooth microtubes, Heat Transfer Eng. 28 (8–9) (2007) 670–679, http://dx.doi.org/10.1080/01457630701326308.
[51] D. Du, Z. Li, Z. Guo, Friction resistance for gas flow in smooth microtubes, Sci. China Ser. E: Technol. Sci. 43 (2) (2000) 171–177, http://dx.doi.org/10.1007/bf02916887.
[52] G.L. Morini, Scaling effects for liquid flows in microchannels, Heat Transfer Eng. 27 (4) (2006), http://dx.doi.org/10.1080/01457630500523865.

[53] T.-Y. Lin, S.G. Kandlikar, A theoretical model for axial heat conduction effects during single-phase flow in microchannels, J. Heat Transfer 134 (2) (2011) 020902, http://dx.doi.org/10.1115/1.4004936.
[54] G. Maranzana, I. Perry, D. Maillet, Mini- and micro-channels: influence of axial conduction in the walls, Int. J. Heat Mass Transfer 47 (17–18) (2004) 3993–4004, http://dx.doi.org/10.1016/j.ijheatmasstransfer.2004.04.016.
[55] G.L. Morini, M. Spiga, The role of the viscous dissipation in heated microchannels, J. Heat Transfer 129 (3) (2006) 308–318, http://dx.doi.org/10.1115/1.2430725.
[56] T.-Y. Lin, S.G. Kandlikar, An experimental investigation of structured roughness effect on heat transfer during single-phase liquid flow at microscale, J. Heat Transfer 134 (10) (2012), http://dx.doi.org/10.1115/1.4006844. pp. 101701-101701.
[57] G. Gamrat, M. Favre-Marinet, S. Le Person, Modelling of roughness effects on heat transfer in thermally fully-developed laminar flows through microchannels, Int. J. Therm. Sci. 48 (12) (2009) 2203–2214, http://dx.doi.org/10.1016/j.ijthermalsci.2009.04.006.
[58] C.V. Thompson, R. Carel, Stress and grain growth in thin films, J. Mech. Phys. Solids 44 (5) (1996) 657–673, http://dx.doi.org/10.1016/0022-5096(96)00022-1.
[59] H.T. Ng, B. Chen, J.E. Koehne, A.M. Cassell, J. Li, J. Han, M. Meyyappan, Growth of carbon nanotubes: a combinatorial method to study the effects of catalysts and underlayers, J. Phys. Chem. B 107 (33) (2003) 8484–8489, http://dx.doi.org/10.1021/jp034198w.
[60] Y. Wang, Z. Luo, B. Li, P.S. Ho, Z. Yao, L. Shi, E.N. Bryan, R.J. Nemanich, Comparison study of catalyst nanoparticle formation and carbon nanotube growth: support effect, J. Appl. Phys. 101 (12) (2007) 124310, http://dx.doi.org/10.1063/1.2749412.
[61] H. Dai, Carbon nanotubes: synthesis, integration, and properties, Acc. Chem. Res. 35 (12) (2002) 1035–1044, http://dx.doi.org/10.1021/ar0101640.
[62] M. Terrones, H. Terrones, The carbon nanocosmos: novel materials for the twenty-first century, 2003.
[63] J.H. Lehman, M. Terrones, E. Mansfield, K.E. Hurst, V. Meunier, Evaluating the characteristics of multiwall carbon nanotubes, Carbon 49 (8) (2011) 2581–2602, http://dx.doi.org/10.1016/j.carbon.2011.03.028.
[64] P. Kim, L. Shi, A. Majumdar, P.L. Mceuen, Thermal transport measurements of individual multiwalled nanotubes, Phys. Rev. Lett. 87 (21) (2001) 215502.
[65] S. Sinha, S. Barjami, G. Iannacchione, A. Schwab, G. Muench, Off-axis thermal properties of carbon nanotube films, J. Nanopart. Res. 7 (6) (2005) 651–657, http://dx.doi.org/10.1007/s11051-005-8382-9.
[66] H. Xie, A. Cai, X. Wang, Thermal diffusivity and conductivity of multiwalled carbon nanotube arrays, Phys. Lett. A 369 (1–2) (2007) 120–123, http://dx.doi.org/10.1016/j.physleta.2007.02.079.
[67] C.D. Meinhart, S.T. Wereley, J.G. Santiago, Piv measurements of a microchannel flow, Exp. Fluids 27 (5) (1999) 414–419, http://dx.doi.org/10.1007/s003480050366.
[68] B. Xu, K.T. Ooti, N.T. Wong, W.K. Choi, Experimental investigation of flow friction for liquid flow in microchannels, Int. Commun. Heat Mass Transfer 27 (8) (2000) 1165–1176, http://dx.doi.org/10.1016/S0735-1933(00)00203-7.
[69] F. Debray, J.P. Franc, Amp.X. Maı, T. Tre, S. Reynaud, Mesure Des Coefficients De Transfert Thermique Par Convection Forcée En Mini-Canaux, Mécanique & Industries 2 (5) (2001) 443–454.
[70] S.E. Turner, H. Sun, M. Faghri, O.J. Gregory, Compressible gas flow through smooth and rough microchannels, Proc. IMECE ASME 2001, HTD-24145), 2001.
[71] R.E. Acosta, R.H. Muller, C.W. Tobias, Transport processes in narrow (capillary) channels, AIChE J. 31 (3) (1985) 473–482, http://dx.doi.org/10.1002/aic.690310315.
[72] S.G. Kandlikar, D. Schmitt, A.L. Carrano, J.B. Taylor, Characterization of surface roughness effects on pressure drop in single-phase flow in minichannels, Phys. Fluids 17 (10) (2005) 100606, http://dx.doi.org/10.1063/1.1896985.
[73] S.G. Kandlikar, Heat Transfer and Fluid Flow in Minichannels and Microchannels, second ed., Single-Phase Liquid Flow in Minichannels and Microchannels, Butterworth-Heinemann, Oxford, 2014. Chapter 3.